

1 **Title**

2 The frequency gradient of human resting-state brain oscillations follows cortical
3 hierarchies.

4 **Author names and affiliations**

5 Keyvan Mahjoory^{1*}, Jan-Mathijs Schoffelen², Anne Keitel³, Joachim Gross^{1,4,5*}

6 Correspondence:

7 kmahjoory@gmail.com (K.M.); joachim.gross@uni-muenster.de (J.G.)

8 ¹Institute for Biomagnetism and Biosignalanalysis (IBB), University of Muenster, 48149,
9 Muenster, Germany.

10 ²Radboud University Nijmegen, Donders Institute for Brain, Cognition and Behaviour,
11 Nijmegen, The Netherlands.

12 ³Psychology, University of Dundee, Scrymgeour Building, Dundee DD1 4HN, UK

13 ⁴Centre for Cognitive Neuroimaging (CCNi), University of Glasgow, Glasgow, UK

14 ⁵Otto-Creutzfeldt-Center for Cognitive and Behavioral Neuroscience, University of
15 Muenster, 48149 Muenster, Germany.

16

17 **Abstract**

18 The human cortex is characterized by local morphological features such as cortical
19 thickness, myelin content, and gene expression that change along the posterior-anterior
20 axis. We investigated if some of these structural gradients are associated with a similar
21 gradient in a prominent feature of brain activity - namely the frequency of oscillations. In
22 resting-state MEG recordings from healthy participants (N=187) using mixed effect
23 models, we found that the dominant peak frequency in a brain area decreases
24 significantly along the posterior-anterior axis following the global hierarchy from early
25 sensory to higher-order areas. This spatial gradient of peak frequency was significantly
26 anticorrelated with that of cortical thickness, representing a proxy of the cortical
27 hierarchical level. This result indicates that the dominant frequency changes
28 systematically and globally along the spatial and hierarchical gradients and establishes
29 a new structure-function relationship pertaining to brain oscillations as a core
30 organization that may underlie hierarchical specialization in the brain.

31 **Introduction**

32 It is well established that the brain's cortical areas differ in their cyto- and
33 myeloarchitectonic structure, local and long range anatomical connectivity, activity and,
34 by consequence, their function (Glasser et al., 2016; Huntenburg et al., 2017).
35 Interestingly, many structural features that distinguish individual brain areas change
36 gradually in an orderly manner across the cortex, leading to spatial feature gradients.
37 The most prominent and best established gradients are evident along the posterior-
38 anterior axis (Eickhoff et al., 2018; Felleman and Van Essen, 1991; Huntenburg et al.,
39 2018). For instance, neuron density decreases and neuronal connectivity increases from
40 posterior to anterior brain areas. These differences have been attributed to differences
41 in neurogenesis for posterior compared to anterior brain areas (Hill et al., 2010;

42 Huntenburg et al., 2018). A similar posterior-anterior gradient has been observed for
43 myelin content, cortical thickness, and gene expression (Burt et al., 2018). Next to the
44 posterior-anterior gradient, other global spatial organization principles have been
45 proposed to explain the variation of microstructural features across the cortex. For
46 instance, Huntenburg et al. suggest a sensorimotor to transmodal gradient as an
47 important intrinsic organizing dimension of human cortex (Huntenburg et al., 2018)
48 reflecting gradual changes in structural features from functionally unimodal (dedicated
49 sensory or motor) areas to higher order, transmodal areas.

50 In addition to structural gradients as an organizing principle reflecting global cortical
51 organization, it is well acknowledged that cortical areas are structurally connected into
52 larger networks, which often display a hierarchical organization. Cortical hierarchies are
53 typically established based on the degree of microstructural differentiation of the
54 connected areas, and on the classification of the anatomical connections as feedforward
55 or feedback using histological tract-tracing. Early sensory areas with predominantly
56 feedforward outgoing connections are placed at the bottom of the hierarchy and higher
57 order association areas with mostly feedback outgoing connections are placed at the top
58 of the hierarchy (Felleman and Van Essen, 1991; Markov et al., 2014). A noninvasive,
59 but indirect index of these hierarchies is cortical thickness, a macroscopic feature of the
60 cortex, which can be estimated from MRI scans. It has been shown that cortical thickness
61 mirrors global hierarchical organization of the cortex as well as local hierarchies in visual,
62 auditory and somatosensory areas (Jasmin et al., 2019; Wagstyl et al., 2015), and,
63 therefore, could be used as a basis for understanding hierarchy-gradient relationships in
64 the cortex.

65 The presence of these anatomical gradients raises the question to what extent they are
66 reflected in features of brain activity and brain function. Indeed, it has been shown that
67 cortical areas follow a hierarchical ordering in their timescales of intrinsic fluctuations as
68 for example measured in the autocorrelation of spiking activity (Murray et al., 2014).

69 Sensory areas show faster fluctuations while frontal areas show slower fluctuations.
70 Shorter timescales in sensory areas enables them to reflect dynamic changes in the
71 environment, whereas the longer timescales in prefrontal areas allows for integration of
72 information. Particularly, this gradient of ‘temporal receptive windows’ has been
73 demonstrated in visual (Himberger et al., 2018) and auditory processing (Jasmin et al.,
74 2019) and could be related to the frequency of spontaneous brain oscillations.
75 Oscillations are a prominent feature of brain activity, and have been suggested to play a
76 central role in coordinating neuronal activity (Fries, 2005; Wang, 2010). Similar to many
77 anatomical features described above, the spectral activity patterns have been shown to
78 be characteristic for each brain area (Keitel and Gross, 2016). This is consistent with the
79 view that the individual anatomical structure of a brain area shapes its rhythmic neuronal
80 activity, which led us to hypothesize the existence of a posterior-anterior gradient in the
81 frequency of spontaneous brain rhythms.

82 Spontaneous rhythms have been studied in the past but typically by focusing on the
83 power in specific frequency bands (Hillebrand et al., 2016; Keitel and Gross, 2016;
84 Mellem et al., 2017). Overall, these MEG studies revealed strongest cortical generators
85 for the dominant alpha rhythm (7–13 Hz) in occipito-parietal brain areas. The beta band
86 (15–30 Hz) shows strongest activity in sensorimotor areas while delta (1–3 Hz) and theta
87 (3–7 Hz) bands are associated with activity in wide-spread areas including frontal cortex.
88 Here, we adopt a different approach that is based on sophisticated identification of
89 spectral peaks in the power spectra of source-localized resting-state MEG data and
90 included modelling of the 1/f spectral background (Haller et al., 2018). This approach
91 offers two distinct advantages. First, focusing on spectral peaks ensures that results are
92 indeed based on brain oscillations. This is not necessarily the case when using the power
93 in a pre-defined frequency band or using band-pass filtered data. Second, by explicitly
94 modelling the 1/f spectral background across the entire cortex we can dissociate

95 contributions due to aperiodic neuronal background activity from those originating from
96 oscillatory activity.

97 We used this approach to specifically test the hypothesis of a posterior-anterior gradient
98 in the frequency of spontaneous brain rhythms. We identified the frequencies of the
99 dominant brain rhythm across the cortex in source-localized resting-state MEG data of
100 187 individuals.

101 As we describe below, we found spatial gradients of the dominant peak frequency
102 across the cortex following the cortical hierarchy.

103 **Results**

104 **Spatial Gradients of the Dominant Peak Frequency of Oscillations**

105 We analyzed publicly available resting-state MEG data from 187 participants (Schoffelen
106 et al., 2019a, 2019b), reconstructing cortical activity time courses for 7,548 dipolar
107 sources located in the cortical surface. We parceled the cortex to 384 regions-of-interest
108 (ROIs) using the cortical parcellation (introduced in (Schoffelen et al., 2017)) constructed
109 from the Conte69 atlas (Van Essen et al., 2012) which divides the cortical surface
110 according to the division introduced by Brodmann (Brodmann, 1909).

111 For each ROI, we concatenated the source time courses of the locations belonging to
112 that ROI and reduced the dimensionality using a singular value decomposition. The
113 obtained components were segmented to 2-second epochs. Power spectra were
114 computed for each epoch, pooled across components, and eventually their 10% trimmed
115 mean was computed to obtain a single spectrum per ROI and individual.

116 Spectral peaks were identified from ROI spectrum after fitting and subtracting the
117 arrhythmic 1/f component (see Figure 1A and method section). Subsequently, we
118 identified for each participant and ROI the spectral peak with strongest amplitude in the
119 original power spectrum (dominant peak frequency, or for simplicity, merely called peak

120 frequency (PF)). We used PF to test our hypothesis of a posterior-anterior frequency
121 gradient.

122 Figure 1B, top panel, shows the distribution of PF as a function of the ROI's location
123 along the y-axis of the coordinate system (posterior to anterior). Each point represents
124 the trimmed mean across participants of the PF for one ROI. A clear gradual decrease
125 of PF from posterior to anterior is evident and supported by a significant correlation
126 (skipped Pearson correlation, Robust Correlation Toolbox) (Pernet et al., 2012) between
127 the trimmed mean PF and the ROI's y-coordinate ($r = -0.84$, $p << 0.001$). This frequency
128 gradient is also evident in the cortical maps that show the trimmed mean of the PF across
129 participants for the 384 ROIs (Figure 1B, bottom panel). At the individual level, we
130 computed the correlation between the Y-coordinates and PF values and found a
131 significant posterior-to-anterior gradient of PF for 84% of participants ($p < 0.05$).
132 Figure 1B, top-right panel, illustrates the distribution of the obtained within-individual
133 correlation values across all individuals and shows consistency but also the variability of
134 this gradient (t -value = -15.52 , $p < 0.001$) across individuals.

135 To account for this inter-individual variability and also assess global, consistent, and
136 systematic changes of PF across the cortical surface along the 3-dimensional space and
137 along the known established cortical hierarchies, we applied a comprehensive statistical
138 model using mixed-effect modeling. Our use of linear-mixed-effect models (LMEM)
139 ensured that the individual differences are properly accounted for and that significant
140 gradients are consistently present in individual participants. For example, participants
141 have different alpha peak frequency in occipital brain areas and the slope of frequency
142 gradient is different. These individual differences are specifically modelled by LMEM as
143 random effects. Importantly, LMEM applies two-level statistics, and therefore, will only
144 show a significant gradient if it is significant across cortical areas at the individual level,
145 and consistent across participants at the group level. We used PF as the response
146 variable, and the coordinates of the ROI centroids (X: left to right, Y: posterior to anterior,

147 and Z: inferior to superior) plus their two-way interactions set as fixed effects. We
148 modelled the individual slope and offset as random effects to account for variability
149 between participants.

150 The fixed effect parameters capture mean-variation in the PF that is shared by all
151 individuals (see Methods section), while the participant-unique variance of the PF is
152 addressed by random effects. Thus, our model provides a robust and comprehensive
153 characterization of spatial changes of PF across the cortex and addresses the confound
154 of inter-individual differences. Figure 1C displays a table of T-values for fixed-effect
155 parameters of LMEM and the modelled PF on the cortex. LMEM yielded highly significant
156 scores for Y ($t = -15.6$, $p << 0.001$), Z ($t = -10.4$, $p << 0.001$), and Y:Z ($t = -32$, $p << 0.001$)
157 directions. Together, these results support the conclusion that the peak frequency of
158 brain oscillations decreases systematically in posterior-anterior direction. Furthermore,
159 LMEM identified a second global axis where PF decreases along the Z axis (inferior-
160 superior direction).

161 On the basis of the observed frequency gradient, the question may arise, whether the
162 spatial pattern of frequency across the cortex is the result of spatial leakage originating
163 from an occipital alpha and frontal theta source. If this is the case, we would not expect
164 to see significant frequency change in areas close to primary visual area (V1). To address
165 this question, we computed the geodesic distance between the reference ROI, V1, and
166 all areas located 2–3 cm away from V1, and applied linear mixed effect modelling of PF
167 as a function of the distance values. We found a highly significant negative dependence
168 between PF and distance ($t = -21.1$, $p << 0.001$).

169 To further account for the potential confounding effect of spatial leakage we performed a
170 new comprehensive analysis, where we computed the geodesic distance between
171 centroid of all ROIs and the centroid of V1 (Figure 1D bottom panel) and used this as a
172 new axis because it well explains the posterior-anterior axis in the cortex. Our analysis
173 showed a significant negative correlation between the trimmed mean PF and the

174 geodesic distance values ($r = -0.89$, $p << 0.001$; Figure 1D top-left panel). This negative
175 correlation was evident at the individual level for 88% of participants ($p < 0.05$) and was
176 consistent across individuals (t -value = -17.32 , $p < 0.001$; Figure 1D top-left panel). To
177 account for this inter-individual variability, we applied an LMEM between the PF as a
178 response variable and the geodesic distance values as an independent variable. We
179 found a highly significant gradient of PF along the specified geodesic distance ($t = -18.9$,
180 $p << 0.001$; Figure 1E, cortical map). Furthermore, to answer the question whether the
181 spatial gradient of PF constantly exists in different areas of the cortex, we split the cortex
182 to 3 equal, consecutive and non-overlapping windows (about 4 cm) based on the Y axis,
183 applied LMEM for each window modelling PF as a function of geodesic distance, and
184 found a significant gradient (window 1: $t = -8.1$, window 2: $t = -10.9$, window 3: $t = -5.2$,
185 all $p < 0.001$) (figure 1E). Indeed, our analysis demonstrates a significant organization of
186 PF along the posterior-anterior direction for all windows indicating that this axis
187 constitutes a systematic and constant gradient of PF.

188

189 ===== Figure 1 about here =====

190

191 **Spatial Gradients of Spectral Properties of the 1/f Signal**

192 Neurophysiological signals typically consist of oscillatory signal components with distinct
193 spectral peaks, embedded in an arrhythmic 1/f signal component. Variation in the
194 properties of this 1/f component may give rise to shifts of spectral peak estimates, and
195 lead to misidentification of peak frequencies (Haller et al., 2018). To investigate this
196 issue, we examined the spatial distribution across the cortex of the estimated slope and
197 offset parameters of the arrhythmic component (see method section), using LME
198 modelling. As illustrated in figures 2A and 2B, we found significant scores for Y (slope: t
199 = -4.3 , $p << 0.001$; offset: $t = 2.8$, $p < 0.01$), Y:Z (slope: $t = 6.9$, $p << 0.001$; offset: $t =$
200 13.2 , $p << 0.001$), and X:Y (slope: $t = -6.8$, $p << 0.001$; offset: $t = -5.8$, $p << 0.001$)

201 directions. These results indicate a significant decrease of the 1/f slope, and an increase
202 of its offset along the posterior-to-anterior direction. The observed similarity between
203 spatial patterns of 1/f parameters and PF, brings up the question to what extent these
204 parameters could contribute to the observed PF gradient. To assess this, we tested to
205 what extent the spatial change of PF is independent of spatial changes of 1/f slope and
206 offset. We thus used LMEM and regressed out the linear contribution of 1/f slope and
207 offset to PF. Then, we again used LMEM to model the residual PF values as a function
208 of spatial coordinates. The results confirmed a significant posterior-anterior gradient of
209 residual PF values (t-values: $Y = -8.3$, $Z = -4.3$, $Y:Z = -16$; all $p << 0.001$, Figures 2C and
210 2D). We therefore conclude that the posterior-anterior PF gradient is largely independent
211 of the observed gradients of slope and offset of the 1/f component.

212

213 ===== Figure 2 about here =====

214

215 **Frequency Gradients follow Cortical Hierarchies**

216 The visual system's cortical hierarchy largely progresses along the posterior-anterior
217 direction, and starts in early visual areas in occipital cortex and progresses along the
218 dorsal and ventral streams to anterior areas. Since this progression of cortical
219 hierarchical level coincides with the observed gradient in PF, we tested the hypothesis
220 that the PF gradient is more closely related to cortical hierarchical level than to spatial
221 location. We used cortical thickness (CT) as a proxy for the quantification of the
222 hierarchical level of brain areas (Valk et al., 2020; Wagstyl et al., 2015).

223 We used Freesurfer to estimate CT as the shortest distance between corresponding
224 vertices on the white matter surface and the pial surface. To obtain a thickness value for
225 each cortical region, the individual thickness scores were averaged across vertices of
226 that region. Figure 3 shows a significant change of mean CT along the posterior-anterior
227 axis ($r = 0.36$, $p << 0.001$, top panel). The bottom panel of Figure 3 depicts CT values

228 averaged across participants and mapped on the cortex. LMEM of CT as a function of
229 ROI coordinates showed a significant and progressive increase of CT from posterior to
230 anterior regions (t-values: $Y = 49.7$, $Z = -29.3$, $Y:Z = 16.2$; all $p << 0.001$). Notably, similar
231 to the spatial gradients of PF, LMEM uncovered a secondary inferior-superior axis of CT.
232 Having established the organizational axes of CT, we then tested for a significant
233 relationship between CT and PF. LMEM ($t = -13.8$, $p << 0.001$) showed a significant
234 negative relationship between PF and CT. Next, we asked the question if this relationship
235 is still significant after removing from both, PF and CT, the effect of ROI coordinates
236 (x,y,z). This was done by modeling the dependencies of PF and CT respectively on ROI
237 coordinates and computing the residuals PFres and CTres. These residuals describe
238 individual spatial variations of PF and CT that cannot be explained by a linear model of
239 their spatial location. PFres and CTres are still significantly related (LMEM: $t = -6.9$, $p <<$
240 0.001 , Figure 3—figure supplement 1) indicating that they are more directly related to
241 each other than can be explained by their individual dependency on location (x,y,z). This
242 result suggests that peak frequency is related to structural features that likely represent
243 cortical hierarchies.

244

245 ===== Figure 3 about here =====

246

247 We further tested the relationship between PF gradients and cortical hierarchies along
248 the anatomically defined and well-established visual hierarchy. Following an approach
249 by Michalareas et al. (Michalareas et al., 2016), we selected seven cortical regions
250 showing strong homology to macaques visual areas (V1, V2, V4, MT, DP, TEO, 7A)
251 using the cortical parcellation of Glasser et al. (Glasser et al., 2016). Figure 4A, top panel
252 displays a schematic representation of the seven regions. We modeled spatial changes
253 of PF along the visual hierarchy, using LMEM (see method section for details), and found
254 a significant decrease of PF ($t = -10.1$, $p << 0.001$). A similar analysis was also performed

255 on CT and found a significant increase of CT along the visual hierarchy ($t = 54.9$, $p << 0.001$). Figure 4A, bottom panel (bars) shows the fixed effects of the LMEM applied
256 separately on PF and CT scores.

257 Previous studies have shown that cortical regions can be contextualized in terms of eight
258 canonical resting-state networks comprising three sensory (visual, somatosensory, and
259 auditory) and five higher-order association networks (frontoparietal, cingulo-opercular,
260 default mode, dorsal attention, and ventral attention; Figure 4B)(Ito et al., 2017). Markers
261 of hierarchical microcircuit specialization such as the ratio of T1-weighted to T2-weighted
262 MRI maps (T1w/T2w) are significantly different between sensory and association areas
263 (Burt et al., 2018; Demirtaş et al., 2019). Here, we extended this approach to our
264 measures to test for differences in PF/CT between sensory and association networks.

265 Following Ito et al. (Ito et al., 2017), we assigned all cortical regions to eight resting-state
266 networks and defined a categorical variable comprising eight labels corresponding to the
267 networks. This categorical variable was used as a fixed effect (independent variable) and
268 the PF/CT as a response variable for an LMEM, to test the effect of networks on cortical
269 organization of PF/CT. The random effect was defined as in equation1. Figure 4B shows
270 the effect of each network (fixed effect) for CT (top panel) and for PF (bottom panel).
271 Error bars indicate the lower and upper bounds of LMEM for the fixed effect. Next, we
272 applied ANOVA on LMEM and found a significant effect of resting-state networks for PF
273 and CT (PF: F -stats = 264, $p << 0.001$; CT: F -stats = 746, $p << 0.001$). Similarly, PF and
274 CT were significantly different between sensory and association areas (LMEM, PF: $t = -$
275 11.1, $p << 0.001$; CT: $t = 14.7$, $p << 0.001$, Figure 4B). As expected, PF is higher in
276 sensory areas compared to association areas while an opposite effect is observed for
277 CT. These results are largely caused by the fact that networks differ in their location and
278 that higher-order associative brain areas are located more anterior compared to sensory
279 brain areas (most prominently in the visual domain). Still, we believe that the 'network
280 representation' of our results is important to emphasize the point that these quantities

282 (PF and CT) differ between networks. This is especially important for studies focusing a-
283 priori on these anatomically defined networks and where these differences may confound
284 other results. However, we also tested if PF and CT differ between networks irrespective
285 of their location. This was done by removing from both measures changes that can be
286 explained by linear dependencies on x,y,z. Interestingly, after regressing out the effect
287 of spatial location, a significant difference among networks remained for PF (Figure 4–
288 figure supplement 1) and CT (Figure 4–figure supplement 2). This was the case when
289 looking at the standard resting-state networks and also when testing sensory against
290 association areas. These results indicate that, beyond a global effect of location,
291 networks still differ significantly in PF and CT after removing the linear effects of location.

292

293 ===== Figure 4 about here =====

294

295 **Spatial Gradients are frequency specific**

296 In the results presented so far, we defined the PF per ROI as the most prominent peak
297 in the spectrum. Some ROIs, however, showed more than a single spectral peak possibly
298 indicating the presence of several gradients. We tested this in four frequency bands
299 derived from our data. Figure 5 shows a histogram (across ROIs and participants) of all
300 detected spectral peaks. Interestingly, this histogram of peak frequencies clearly
301 delineates the classical frequency bands that are traditionally used in the EEG and MEG
302 literature – but they are here derived in a purely data-driven manner (4–7.5 Hz (theta),
303 8.5–13 Hz (alpha), 15–25 Hz (low beta) 27.5–34 Hz (high beta), for subsequent analysis
304 both beta bands were combined).

305

306 ===== Figure 5 about here =====

307

308 We identified the band-specific PF as the frequency of the peak with largest amplitude in
309 a given frequency band for each ROI and participant. Analogous to the PF analysis, we
310 used LMEM to model band-specific PF as a function of the ROIs' coordinates (Figure 6).
311 We found a significant decrease of alpha peak frequency (correlation with y-axis: $r = -$
312 0.87 , $p << 0.001$; LMEM: $Y, t = -10, p << 0.001; = Y:Z, t = 3.2, p = 0.001$, figures 6B and
313 6E) only along the posterior-anterior direction, while theta- (correlation with y-axis: $r =$
314 0.40 , $p < 0.001$; LMEM: $Y, t = 7.4, p << .0.001; Z, t = -7, p << 0.001; Y:Z, t = -8, p <<$
315 0.001 , figures 6A and 6D) and beta-range (correlation with y-axis: $r = 0.9$, $p << 0.001$;
316 LMEM: $Y, t = 9.3, p << 0.001; Z, t = 4.7, p << 0.001; Y:Z, t = 2.3, p << 0.001$, figures 6C
317 and 6F) frequencies significantly increased along the same direction. Moreover, LMEM
318 identified a secondary significant gradient of theta- and beta-PF along the z-axis.
319 This spatial gradient of band-specific PFs was independent of spatial changes of 1/f slope
320 and offset (Figures 6–figure supplement 1) but significantly correlated with that of CT
321 scores (Figure 6–figure supplement 2).

322

323 ===== Figure 6 about here =====

324

325 **Discussion**

326 This study is the first comprehensive demonstration of frequency gradients across the
327 human cortex using a large set of resting-state MEG recordings. We found that the
328 dominant peak frequency in a brain area decreases significantly, gradually and robustly
329 along the posterior-anterior axis, following the global cortical hierarchy from early sensory
330 to higher order areas. This finding establishes a frequency gradient of resting-state brain
331 rhythms that complements previous anatomical studies reporting a posterior-anterior
332 gradient in microscale and macroscale anatomical features of animal and human cortex
333 (Huntenburg et al., 2018).

334 Several MEG/EEG studies have demonstrated that alpha activity (~10 Hz) is strongest
335 in occipito-parietal brain areas and theta activity (~5 Hz) strongest in more frontal brain
336 areas (Chiang et al., 2011; Voytek et al., 2010). There is also evidence that the dominant
337 frequencies differ between brain areas (Groppe et al., 2013; Hillebrand et al., 2016; Keitel
338 and Gross, 2016). However, we provide the first comprehensive (in frequency and space)
339 statistical model of frequency gradients in a large resting-state brain activity.
340 Our results are consistent with a recent invasive study showing a systematic decrease
341 of peak frequency from posterior to anterior brain areas in ECoG recordings of epilepsy
342 patients (Zhang et al., 2018).
343 A differentiating feature of our approach was that we used a large number of healthy
344 participants ($N = 187$), reconstructed cortical activity from noninvasive MEG recordings,
345 and considered further anatomical features (i.e. cortical thickness). Notably, estimating
346 the power spectrum in finely parcellated ROIs allowed us an accurate and robust
347 identification of peak frequencies and characterization of their spatial gradients across
348 the entire cortical surface. Importantly, we focus on peaks in the power spectrum that
349 indicate the presence of rhythmicity in the neuronal activity, instead of focusing on
350 predefined frequency bands where these rhythms might be absent. As slope and offset
351 of frequency gradient could dramatically vary across participants, averaging across
352 participants may not yield a reliable representation of PF gradient. Instead, we used
353 mixed effect modelling of PF along the cortical hierarchies, where the between-
354 participant variability was taken into account as a random effect. For example, the peak
355 frequency in occipital brain areas and the slope of the frequency gradient varies across
356 individuals, and thus the intercept and slope of the corresponding least square fit change.
357 These individual differences are specifically modelled by a mixed effect model as random
358 effects. Importantly, a mixed effect model will only show a significant gradient if it is
359 significant across cortical areas at the individual level, and consistent across participants
360 at the group level.

361 Results of our analyses showed that, just as peak frequency significantly decreased
362 along the posterior-anterior axis, CT significantly increased in the same direction, which
363 resulted in a significant anticorrelation between PF and CT. The observed correlation
364 holds after removing the effect of spatial location (x,y,z). This seems to indicate that PF
365 and CT are more closely related to each other than can be explained by spatial location
366 alone. Since cortical hierarchies do not strictly follow a single linear trajectory in space
367 (e.g. posterior-anterior) our results are consistent with the idea that both PF and CT,
368 follow cortical hierarchies. Indeed, such local spatial gradients have been reported in
369 multiple features of cortex during auditory perception (Jasmin et al., 2019) and visual
370 processing streams (Himberger et al., 2018). From a broader view, local gradients could
371 mirror complex organization of gradients in human cortex and support the approach of
372 global gradient along the sensory to transmodal areas (Huntenburg et al., 2018). On the
373 other hand, posterior-anterior gradient of PF was significant after subtracting CT scores
374 from PF values. This suggests a partial independence of both measures. Since PF is a
375 measure derived from brain activity the reported gradient could be modulated
376 dynamically depending on cognitive state or task demands. Further studies are needed
377 to investigate this in more detail.

378 We further addressed the question if our results can be explained by the linear
379 superposition of activity from an occipital alpha source and a frontal theta source. Along
380 the posterior-anterior axis, differential superposition of both sources could lead to a
381 frequency gradient, due to imperfect unmixing of the signals. However, our analysis
382 revealed that a significant frequency gradient is already evident within 2–3 cm of V1
383 where the effect of a frontal theta source (which has on average a lower power compared
384 to occipital alpha) is negligible. Furthermore, A more comprehensive analysis showed
385 existence of this gradient for posterio-parietal, central, and frontal areas, separately,
386 acknowledging the globally and continuously decreasing nature of the posterior-anterior
387 gradient.

388 Additional supporting evidence can be drawn from intracranial studies, where the data is
389 directly recorded from cortex. Zhang et al. (Zhang et al., 2018) have shown that
390 oscillations generally propagate in a posterior-to-anterior direction because they are
391 coordinated by an overall decrease in intrinsic oscillation frequency from posterior to
392 anterior regions (see figures S6 and 7 of (Zhang et al., 2018)). Overall, this indicates the
393 existence of a gradual decrease of PF along the posterior-anterior axis.

394 What is the potential functional role of this frequency gradient? Zhang et al. demonstrated
395 the existence of travelling waves along the frequency gradient (Zhang et al., 2018).
396 Interestingly, they found that local frequencies along the posterior-to-anterior direction
397 are positively correlated with waves' propagation speed and direction consistent with a
398 proposed model of travelling waves based on weakly coupled oscillators (WCO)
399 (Ermentrout and Kleinfeld, 2001). Travelling waves along the posterior-anterior axis have
400 also been reported during visual stimulation (Alamia and VanRullen, 2019; Lozano-
401 Soldevilla and VanRullen, 2019). These travelling waves might serve to drive neural
402 communication along the cortical hierarchy possibly through nested gamma oscillations
403 thereby linking travelling waves to the concept of pulsed inhibition (Bahramisharif et al.,
404 2013). In addition, travelling waves have been associated with memory consolidation and
405 learning (Muller et al., 2018). It is of interest to note that frequency gradients have been
406 reported previously in the entorhinal cortex (Giocomo et al., 2011; Giocomo and
407 Hasselmo, 2009). Here, a frequency decrease and corresponding travelling waves have
408 been observed in the dorsal-ventral direction and have been related to a representational
409 gradient of spatial scales from coarse to fine (Muller et al., 2018). Indeed, converging
410 evidence across recording methods, species and cortical domains suggests that
411 representations become more 'integrated' with decreasing 'dominant' frequency of the
412 underlying neuronal population. A prime example is the auditory cortex where response
413 latencies and complexity of processing increase along the posterior-anterior axis (Jasmin
414 et al., 2019). This is also mirrored by an increase in cortical thickness and increased ratio

415 of feedback to feedforward connections along this axis. Similar observations have been
416 made across more widely distributed cortical areas where timescales of intrinsic
417 fluctuations in spiking activity increase from posterior to anterior brain areas (Murray et
418 al., 2014). Not surprisingly, these time scales are largely determined by the time
419 constants of synaptic transmission (Duarte et al., 2017). But interestingly, in a
420 computational model of activity in macaque cortex using anatomical connectivity a
421 gradient of time scales also emerges with short, transient responses to input in sensory
422 areas and slower, sustained responses in higher-order areas (Chaudhuri et al., 2015)
423 (see also (Kiebel et al., 2008)).

424 Our approach additionally revealed that cortical peak frequencies decrease
425 systematically along the inferior-superior axis. As seen in Figure 1 this seems to result
426 from the fact that higher-order frontal areas with lower PF have higher z-coordinates
427 compared to the early sensory areas with higher PF. A similar inferior-superior gradient
428 was also observed for cortical thickness. This finding is supported by a recent study
429 reporting an inferior-superior gradient organization of the CT in human and macaque
430 monkeys (Valk et al., 2020), and has been attributed to the organization patterns
431 expected based on the theory of dual origin (Goulas et al., 2018).

432 Our detailed analysis was based on the cortical ROIs' spectral peak with strongest power
433 (PF). However, we identified all peaks in the power spectrum of each ROI. Since spectral
434 peaks indicate the presence of brain rhythms, this data represents a comprehensive
435 overview of these rhythms across the cortex. The histogram of spectral peaks across
436 ROIs and participants provided a data-driven definition of frequency bands. Interestingly,
437 the histogram delineates the classical frequency bands with histogram peaks centering
438 at 4–7.5 (theta), 8.5–13 (alpha), 15–25 (low-beta) 27.5–34 (high-beta) (see figure 5). This
439 is the first MEG study to our knowledge to identify frequency bands from peak
440 frequencies in a large data set (see (Groppe et al., 2013) for a similar approach in a
441 smaller sample of ECoG data).

442 We further analyzed these specific frequency bands for gradients and found significant
443 posterior-anterior frequency changes in the theta, alpha and beta frequency band.
444 Results in the alpha band mirrored the previous results based on the overall strongest
445 peak frequency. Interestingly, and in contrast to the alpha band, peak frequencies
446 increased along the posterior-anterior direction in the theta and beta frequency band. In
447 the model used by Zhang et al. this would correspond to travelling waves from anterior
448 to posterior brain areas (Zhang et al., 2018) that might represent frequency channels for
449 top-down effects (Michalareas et al., 2016; Wang, 2010).

450 An alternative explanation for the observed posterior-to-anterior or anterior-to-posterior
451 changes of the band-specific PFs may come from the laminar organization of the cortex,
452 where several layers exhibit distinct frequency profiles (Bastos et al., 2018) and thickness
453 patterns (Wagstyl et al., 2020). In particular, similar to our results for the spatial gradients
454 of band-specific PFs, Wagstyl and colleagues (Wagstyl et al., 2020) have identified both
455 increasing and decreasing gradients of thickness along the posterior-anterior axis for
456 cortical layers, in the somatosensory, auditory, and motor cortex (see Figure 6 of
457 (Wagstyl et al., 2020)).

458 In summary, our findings show that peak frequencies of cortical areas form a spatial
459 gradient, which follows the global posterior-anterior hierarchy as well as local anatomical
460 hierarchies. Previous research also points to spatial gradients in multiple features of the
461 human and animal cortex. Further research might explore implications of frequency
462 gradients in different cognitive states, disease, and aging.

463 **Materials and Methods**

464 **Experimental Design**

465 In this study we used the MOUS dataset (Schoffelen et al., 2019a, 2019b)
466 (https://data.donders.ru.nl/collections/di/dccn/DSC_3011020.09_236?1) which, among
467 others, contains five minutes of resting state MEG recordings that is available for 197 out

468 of a total of 204 healthy participants (age: mean = 22, range = 18–32, gender: 94
469 females). The participants were instructed to think of nothing specific while focusing on
470 the fixation cross at the center of the screen. Data was collected using a CTF 275-
471 channel radial gradiometer system, and sampled at 1200 Hz (0-300 Hz bandpass), and
472 additional 29 reference channels for noise cancellation purposes.

473 The anatomical images of the head were obtained with a SIEMENS Trio 3T scanner
474 using a T1-weighted magnetization-prepared rapid gradient-echo (MP-RAGE) pulse
475 sequence, with the following parameters: volume TR = 2300 ms, TE = 3.03 ms, 8 degree
476 flip-angle, 1 slab, slice-matrix size = 256 × 256, slice thickness = 1 mm, field of view =
477 256 mm, isotropic voxel-size = 1.0 × 1.0 × 1.0 mm.

478 After removing 10 participants containing excessive ocular-, muscular-, and cardiac-
479 related artefacts, or lacking any visible spectral peak in source space, we used 187
480 participants for our analyses.

481 **MEG Preprocessing**

482 All preprocessing analyses were performed using the Fieldtrip package (Oostenveld et
483 al., 2011). Gradiometer signals were converted to synthetic third-order gradients, high-
484 pass filtered at 0.5 Hz, and low-pass filtered at 140 Hz (Butterworth, 4th order). Line
485 noise was rejected using a DFT filter at 50 and 100 Hz. After down-sampling the data to
486 300 Hz, outlier channels/time segments were rejected using visual inspection of their
487 time course, spectrum and topography. Next, we used independent component analysis
488 (ICA) to identify and remove signal components related to eye blinks/movements and
489 cardiac activity. To this end, we performed ICA, using the infomax algorithm (Bell and
490 Sejnowski, 1995), on a 30-dimensional signal subspace, for computational efficiency. ICs
491 related to artifacts were identified based on their spatial topography and signal time
492 course, and the identified spatial topographies were projected out of the sensor data.
493 This resulted in 3.7 components on average to be rejected (range 1–6).

494 **MRI Analysis**

495 From T1-weighted anatomical images of participants, brain/skull boundary and cortical
496 surfaces (white matter and pial matter) were generated using SPM (Penny et al., 2011)
497 and Freesurfer (version 5.1)(<http://surfer.nmr.mgh.harvard.edu>). The cortical surface
498 was coregistered to a template with a surface-based coregistration approach (Caret
499 software, <http://brainvis.wustl.edu/wiki/index.php/Caret:Download>), and downsampled to
500 8,196 vertices (MNE software, martinos.org/mne/stable/index.html). Using the Caret
501 software, the mid-thickness cortical surface (halfway between the pial and white matter
502 surfaces) was generated. The cortex surface was parceled into 384 ROIs (192 per
503 hemisphere) according to Schoffelen et al. (Schoffelen et al., 2017). 648 vertices located
504 in the medial wall (sub-cortical areas) were excluded from further analysis.
505 The centroid of each parcel was specified as the vertex located at minimum geodesic
506 distance from all other vertices of that parcel.

507 **Source Reconstruction**

508 Source reconstruction was performed using the linearly constrained minimum variance
509 beamformer approach (Van Veen et al., 1997), where the lambda regularization
510 parameter was set to 5%. This approach estimates a spatial filter for each location of a
511 set of defined dipole locations (here: each of the 7,548 non-midline vertices of the mid-
512 thickness cortical mesh), based on the forward model of that location and the sensor
513 covariance matrix. The forward model was computed using the ‘singleshell’ method, with
514 the brain/skull boundary as volume conduction model of the head. The sensor covariance
515 matrix was computed between all MEG-sensor pairs, as the average covariance matrix
516 across the 2-second time window covariance estimates.

517 **ROI Spectrum**

518 For each anatomical ROI, we performed dimensionality reduction using singular value
519 decomposition (svd) on all vertex timeseries. We retained the required number of
520 components to account for 95% of the variance for each ROI (typically 15 components).
521 Component time courses were segmented to two-second epochs, from which power

522 spectra were computed using a multitapered Fast Fourier transform, using discrete
523 prolate spheroidal sequences (dpss) as windowing function, with 2 Hz spectral
524 smoothing. To obtain a single spectrum for each ROI (ROI spectrum), we pooled spectra
525 of epochs across components and computed the 10% trimmed mean across them.
526 Averaging after leaving out 10% of data from left and right tails of the spectra distribution
527 offers a more robust estimate.

528 **Peak Frequency (PF) Detection**

529 We estimated 1/f component of spectrum between 3 and 45 Hz using the FOOOF
530 algorithm (Haller et al., 2018). The algorithm fits a linear approximation of 1/f in log-log
531 spectrum and computes the corresponding slope and offset parameters. Next, we
532 subtracted the estimated 1/f component from the spectrum to obtain a 1/f corrected
533 spectrum per ROI. To identify spectral peaks, we used the MATLAB “findpeaks” function.
534 We extracted all peaks but most of the analysis is based on the peak frequency with the
535 strongest power in the original spectrum that includes the 1/f background.

536 **Cortical Thickness (CT)**

537 We used the Freesurfer package to obtain estimates of CT scores. The CT value of a
538 vertex was computed as the distance between corresponding white matter and pial
539 surface vertices. To obtain thickness values of a ROI, we averaged CT across the
540 vertices of that ROI.

541 **Statistical Analysis**

542 As described above, we computed PF values for 384 ROIs (197 ROIs per hemisphere)
543 of 187 participants. In our statistical analyses, we aimed to investigate the
544 spatial/hierarchical organization of PF across the human cortex, but also control for the
545 between-participant variability. To meet this purpose, we used linear mixed effect
546 modeling (LMM). The distinctive feature of LMMs is that a response variable is
547 modeled as a linear combination of 1) population characteristics that are assumed to be

548 shared by all individuals (fixed effects), and 2) participant-specific effects, that are unique
549 to a particular individual in the population (random effects).

550 To investigate the spatial organization of PFs across the cortex, we specified the PF as
551 response variable and the coordinates of ROI centroids (X: left to right, Y: posterior to
552 anterior, and Z: inferior to superior) plus their two-way interactions (XY, XZ, YX) as fixed
553 effects. The inclusion of two-way interaction as predictors allows the model to adapt well
554 to the cortex geometry. As our random structure, we nested the PFs within participants
555 as well as within hemispheres to account for the variability between participants and
556 hemispheres. Equation 1 shows the specified LMEM

557
$$PF_j = b_0 + S_{0j} + (b_1 + S_{1j})X + (b_2 + S_{2j})Y + (b_3 + S_{3j})Z + b_4XY + b_5XZ + b_6YZ + e_j \quad (1)$$

558 where the response variable PF for the participant j is related to baseline level via (b_0
559), to ROI centroids (fixed effects) via ($b_i, i \in \{1,2,\dots,6\}$), and to error ($e_j \sim N(0, \sigma^2)$). To
560 address the variation of predictors for participant j , we specified both random intercepts
561 (S_{0j}) and slopes ($S_{ij}, i \in \{1,2,3\}$) for random effects. For the sake of model simplicity, no
562 random effect was specified for two-way interactions. We estimated the fixed effect
563 predictions for a ROI located at centroid coordinates of (x, y, z) as follows

564
$$\square \quad PF_{xyz} = b_0 + b_1x + b_2y + b_3z + b_4xy + b_5xz + b_6yz \quad (2)$$

565 In our analysis we included only significant predictors for equation 2. We used an
566 analogous approach, to test the significance of spatial changes of CT and 1/f parameters
567 across the cortex.

568 To examine if the spatial distribution of PF across the cortex is independent of the spatial
569 changes of 1/f parameters (slope and offset), we fitted a LMEM, where we set the PF as
570 a response variable, the 1/f slope and offset scores as fixed effects, and the between-
571 participant and hemisphere as random effects. Prior to LMEM, we standardized the PF,
572 1/f slope and offset scores for each participant by subtracting mean and dividing by
573 standard deviation (z-score). Next, we estimated the coefficients for the fixed effects (1/f

574 parameters) and regressed them out to obtain the residual PF (PFres) scores, which
575 reflect a subspace of PF that cannot be explained by 1/f parameters. We again modeled
576 the obtained PFres scores as a function of ROI centroids as described above (see
577 equation 1).

578 To obtain the correlation between PF and CT scores, we initially computed the 10%
579 trimmed mean across participants for each ROI and performed a robust correlation
580 (skipped Pearson correlation, Robust Correlation Toolbox) (Pernet et al., 2012) between
581 the trimmed mean values. To address the between-participant variability, we first
582 standardized PF and CT scores (as described above), and conducted LMEM, where we
583 specified the PF as response variable and the CT as a fixed effect predictor. The random
584 effect was set according to equation 1. Moreover, we aimed to obtain a correlation value
585 between PF and CT that is independent of spatial location. We first applied LMEM
586 separately for PF and CT, modeling each as a function of ROI coordinates (see equation
587 1), and computed the corresponding residuals (PFres and CTres) for each ROI and
588 participant. Subsequently, we applied LMEM between PFres and CTres values
589 (analogous to PF and CT).

590 To test for the significance of PF changes along the established visual hierarchy
591 comprising seven regions (V1, V2, V4, MT, DP, TEO, 7A), chosen according to
592 Michalareas et al. (Michalareas et al., 2016), we used an LMEM. To impose the
593 hierarchical order of those seven ROIs in our LMEM, we defined a seven-element
594 hierarchy vector for each participant and hemisphere ($V = [1, 2, 3, \dots, 7]$) whose elements
595 refer to the hierarchical level of the corresponding ROI. The random effect was specified
596 as in equation 1. PF values were standardized before LMEM analysis. This model tests
597 the significance of PF changes along the specified hierarchy. An analogous analysis was
598 applied to CT scores of those seven ROIs.

599 To statistically assess the effect of eight resting-state networks on PF, we used a recently
600 released multi-modal parcellation of the human cortex (Glasser et al., 2016) and

601 assigned cortical regions to eight functional resting-state networks comprising three
602 sensory ('VIS', visual; 'AUD', auditory; and 'SOM', somatomotor) and five association
603 ('DAN', dorsal 670 attention; 'FPN', frontoparietal; 'VAN', ventral attention; 'DMN', default
604 mode; and 'CON', cingulo-opercular) networks (Ito et al., 2017). Next, we used an LMEM
605 analysis, where we specified the PF per region and individual as a response variable,
606 and the assigned label for each region ({'VIS', 'AUD', 'SOM', 'DAN', 'FPN', 'VAN', 'DMN',
607 'CON'}) as an independent (categorical) variable. The random structure was defined as
608 in equation 1. This analysis obtains t-values for each network representing the significant
609 effect of that network on PF. Subsequently, we applied ANOVA on LMEM fit and
610 computed F-stat for the fixed effect. A similar analysis was performed to test the effect of
611 resting-state networks on CT scores.

612 All statistical analyses were conducted in Matlab version 9.5 (R2018b). We used the
613 "fitlme" function to perform the LMEM analysis.

614 **Data availability:** All data used for this study are publicly available
615 (https://data.donders.ru.nl/collections/di/dccn/DSC_3011020.09_236?1).

616 **Acknowledgments**

617 The authors would like to thank Peter Hagoort, who initiated and financed the MOUS
618 project, as well as the MOUS-team that collected, and made publicly available, the data
619 used for this study. JG was supported by Interdisciplinary Center for Clinical Research
620 (IZKF) of the medical faculty of Münster (Gro3/001/19) and by the DFG (GR 2024/5-1).

621 **Competing Interests**

622 The authors declare that they have no competing interests.

623 **References**

624 Alamia, A., VanRullen, R., 2019. Alpha oscillations and traveling waves: Signatures of
625 predictive coding? PLoS Biol. 17, e3000487. doi:10.1371/journal.pbio.3000487

- 626 Bahramisharif, A., van Gerven, M.A.J., Aarnoutse, E.J., Mercier, M.R., Schwartz, T.H.,
627 Foxe, J.J., Ramsey, N.F., Jensen, O., 2013. Propagating neocortical gamma
628 bursts are coordinated by traveling alpha waves. *J. Neurosci.* 33, 18849–18854.
629 doi:10.1523/JNEUROSCI.2455-13.2013
- 630 Bastos, A.M., Loonis, R., Kornblith, S., Lundqvist, M., Miller, E.K., 2018. Laminar
631 recordings in frontal cortex suggest distinct layers for maintenance and control of
632 working memory. *Proc. Natl. Acad. Sci. USA* 115, 1117–1122.
633 doi:10.1073/pnas.1710323115
- 634 Bell, A.J., Sejnowski, T.J., 1995. An information-maximization approach to blind
635 separation and blind deconvolution. *Neural Comput.* 7, 1129–1159.
636 doi:10.1162/neco.1995.7.6.1129
- 637 Brodmann, K., 1909. Vergleichende Lokalisationslehre der Grosshirnrinde in ihren
638 Prinzipien dargestellt auf Grund des Zellenbaues. Barth.
- 639 Burt, J.B., Demirtaş, M., Eckner, W.J., Navejar, N.M., Ji, J.L., Martin, W.J., Bernacchia,
640 A., Anticevic, A., Murray, J.D., 2018. Hierarchy of transcriptomic specialization
641 across human cortex captured by structural neuroimaging topography. *Nat.*
642 *Neurosci.* 21, 1251–1259. doi:10.1038/s41593-018-0195-0
- 643 Chaudhuri, R., Knoblauch, K., Gariel, M.-A., Kennedy, H., Wang, X.-J., 2015. A Large-
644 Scale Circuit Mechanism for Hierarchical Dynamical Processing in the Primate
645 Cortex. *Neuron* 88, 419–431. doi:10.1016/j.neuron.2015.09.008
- 646 Chiang, A.K.I., Rennie, C.J., Robinson, P.A., van Albada, S.J., Kerr, C.C., 2011. Age
647 trends and sex differences of alpha rhythms including split alpha peaks. *Clin.*
648 *Neurophysiol.* 122, 1505–1517. doi:10.1016/j.clinph.2011.01.040
- 649 Demirtaş, M., Burt, J.B., Helmer, M., Ji, J.L., Adkinson, B.D., Glasser, M.F., Van Essen,
650 D.C., Sotiropoulos, S.N., Anticevic, A., Murray, J.D., 2019. Hierarchical
651 Heterogeneity across Human Cortex Shapes Large-Scale Neural Dynamics.
652 *Neuron* 101, 1181–1194.e13. doi:10.1016/j.neuron.2019.01.017
- 653 Duarte, R., Seeholzer, A., Zilles, K., Morrison, A., 2017. Synaptic patterning and the
654 timescales of cortical dynamics. *Curr. Opin. Neurobiol.* 43, 156–165.
655 doi:10.1016/j.conb.2017.02.007
- 656 Eickhoff, S.B., Constable, R.T., Yeo, B.T.T., 2018. Topographic organization of the
657 cerebral cortex and brain cartography. *Neuroimage* 170, 332–347.
658 doi:10.1016/j.neuroimage.2017.02.018
- 659 Ermentrout, G.B., Kleinfeld, D., 2001. Traveling electrical waves in cortex: insights from
660 phase dynamics and speculation on a computational role. *Neuron* 29, 33–44.
661 doi:10.1016/s0896-6273(01)00178-7

- 662 Felleman, D.J., Van Essen, D.C., 1991. Distributed hierarchical processing in the
663 primate cerebral cortex. *Cereb. Cortex* 1, 1–47. doi:10.1093/cercor/1.1.1
- 664 Fries, P., 2005. A mechanism for cognitive dynamics: neuronal communication through
665 neuronal coherence. *Trends Cogn. Sci. (Regul. Ed.)* 9, 474–480.
666 doi:10.1016/j.tics.2005.08.011
- 667 Giocomo, L.M., Hasselmo, M.E., 2009. Knock-out of HCN1 subunit flattens dorsal-
668 ventral frequency gradient of medial entorhinal neurons in adult mice. *J.*
669 *Neurosci.* 29, 7625–7630. doi:10.1523/JNEUROSCI.0609-09.2009
- 670 Giocomo, L.M., Moser, M.-B., Moser, E.I., 2011. Computational models of grid cells.
671 *Neuron* 71, 589–603. doi:10.1016/j.neuron.2011.07.023
- 672 Glasser, M.F., Coalson, T.S., Robinson, E.C., Hacker, C.D., Harwell, J., Yacoub, E.,
673 Ugurbil, K., Andersson, J., Beckmann, C.F., Jenkinson, M., Smith, S.M., Van
674 Essen, D.C., 2016. A multi-modal parcellation of human cerebral cortex. *Nature*
675 536, 171–178. doi:10.1038/nature18933
- 676 Goulas, A., Zilles, K., Hilgetag, C.C., 2018. Cortical gradients and laminar projections in
677 mammals. *Trends Neurosci.* 41, 775–788. doi:10.1016/j.tins.2018.06.003
- 678 Groppe, D.M., Bickel, S., Keller, C.J., Jain, S.K., Hwang, S.T., Harden, C., Mehta, A.D.,
679 2013. Dominant frequencies of resting human brain activity as measured by the
680 electrocorticogram. *Neuroimage* 79, 223–233.
681 doi:10.1016/j.neuroimage.2013.04.044
- 682 Haller, M., Donoghue, T., Peterson, E., Varma, P., Sebastian, P., Gao, R., Noto, T.,
683 Knight, R.T., Shestyuk, A., Voytek, B., 2018. Parameterizing neural power
684 spectra. *BioRxiv*. doi:10.1101/299859
- 685 Hill, J., Inder, T., Neil, J., Dierker, D., Harwell, J., Van Essen, D., 2010. Similar patterns
686 of cortical expansion during human development and evolution. *Proc. Natl.*
687 *Acad. Sci. USA* 107, 13135–13140. doi:10.1073/pnas.1001229107
- 688 Hillebrand, A., Tewarie, P., van Dellen, E., Yu, M., Carbo, E.W.S., Douw, L., Gouw,
689 A.A., van Straaten, E.C.W., Stam, C.J., 2016. Direction of information flow in
690 large-scale resting-state networks is frequency-dependent. *Proc. Natl. Acad. Sci.*
691 *USA* 113, 3867–3872. doi:10.1073/pnas.1515657113
- 692 Himberger, K.D., Chien, H.-Y., Honey, C.J., 2018. Principles of temporal processing
693 across the cortical hierarchy. *Neuroscience* 389, 161–174.
694 doi:10.1016/j.neuroscience.2018.04.030
- 695 Huntenburg, J.M., Bazin, P.-L., Goulas, A., Tardif, C.L., Villringer, A., Margulies, D.S.,
696 2017. A systematic relationship between functional connectivity and intracortical

- 697 myelin in the human cerebral cortex. *Cereb. Cortex* 27, 981–997.
698 doi:10.1093/cercor/bhx030
- 699 Huntenburg, J.M., Bazin, P.-L., Margulies, D.S., 2018. Large-Scale Gradients in Human
700 Cortical Organization. *Trends Cogn. Sci. (Regul. Ed.)* 22, 21–31.
701 doi:10.1016/j.tics.2017.11.002
- 702 Ito, T., Kulkarni, K.R., Schultz, D.H., Mill, R.D., Chen, R.H., Solomyak, L.I., Cole, M.W.,
703 2017. Cognitive task information is transferred between brain regions via resting-
704 state network topology. *Nat. Commun.* 8, 1027. doi:10.1038/s41467-017-01000-
705 w
- 706 Jasmin, K., Lima, C.F., Scott, S.K., 2019. Understanding rostral-caudal auditory cortex
707 contributions to auditory perception. *Nat. Rev. Neurosci.* 20, 425–434.
708 doi:10.1038/s41583-019-0160-2
- 709 Keitel, A., Gross, J., 2016. Individual Human Brain Areas Can Be Identified from Their
710 Characteristic Spectral Activation Fingerprints. *PLoS Biol.* 14, e1002498.
711 doi:10.1371/journal.pbio.1002498
- 712 Kiebel, S.J., Daunizeau, J., Friston, K.J., 2008. A hierarchy of time-scales and the
713 brain. *PLoS Comput. Biol.* 4, e1000209. doi:10.1371/journal.pcbi.1000209
- 714 Lozano-Soldevilla, D., VanRullen, R., 2019. The Hidden Spatial Dimension of Alpha:
715 10-Hz Perceptual Echoes Propagate as Periodic Traveling Waves in the Human
716 Brain. *Cell Rep.* 26, 374–380.e4. doi:10.1016/j.celrep.2018.12.058
- 717 Markov, N.T., Vezoli, J., Chameau, P., Falchier, A., Quilodran, R., Huissoud, C., Lamy,
718 C., Misery, P., Giroud, P., Ullman, S., Barone, P., Dehay, C., Knoblauch, K.,
719 Kennedy, H., 2014. Anatomy of hierarchy: feedforward and feedback pathways
720 in macaque visual cortex. *J. Comp. Neurol.* 522, 225–259.
721 doi:10.1002/cne.23458
- 722 Mellem, M.S., Wohltjen, S., Gotts, S.J., Ghuman, A.S., Martin, A., 2017. Intrinsic
723 frequency biases and profiles across human cortex. *J. Neurophysiol.* 118, 2853–
724 2864. doi:10.1152/jn.00061.2017
- 725 Michalareas, G., Vezoli, J., van Pelt, S., Schoffelen, J.-M., Kennedy, H., Fries, P., 2016.
726 Alpha-Beta and Gamma Rhythms Subserve Feedback and Feedforward
727 Influences among Human Visual Cortical Areas. *Neuron* 89, 384–397.
728 doi:10.1016/j.neuron.2015.12.018
- 729 Muller, L., Chavane, F., Reynolds, J., Sejnowski, T.J., 2018. Cortical travelling waves:
730 mechanisms and computational principles. *Nat. Rev. Neurosci.* 19, 255–268.
731 doi:10.1038/nrn.2018.20

- 732 Murray, J.D., Bernacchia, A., Freedman, D.J., Romo, R., Wallis, J.D., Cai, X., Padoa-
733 Schioppa, C., Pasternak, T., Seo, H., Lee, D., Wang, X.-J., 2014. A hierarchy of
734 intrinsic timescales across primate cortex. *Nat. Neurosci.* 17, 1661–1663.
735 doi:10.1038/nn.3862
- 736 Oostenveld, R., Fries, P., Maris, E., Schoffelen, J.-M., 2011. FieldTrip: Open source
737 software for advanced analysis of MEG, EEG, and invasive electrophysiological
738 data. *Comput Intell Neurosci* 2011, 156869. doi:10.1155/2011/156869
- 739 Penny, W.D., Friston, K.J., Ashburner, J.T., Kiebel, S.J., Nichols, T.E., 2011. Statistical
740 parametric mapping: the analysis of functional brain images. Elsevier.
- 741 Pernet, C.R., Wilcox, R., Rousselet, G.A., 2012. Robust correlation analyses: false
742 positive and power validation using a new open source matlab toolbox. *Front.*
743 *Psychol.* 3, 606. doi:10.3389/fpsyg.2012.00606
- 744 Schoffelen, J.M., Hultén, A., Lam, N., Marquand, A.F., Uddén, J., Hagoort, P., 2017.
745 Frequency-specific directed interactions in the human brain network for
746 language. *Proc. Natl. Acad. Sci. USA* 114, 8083–8088.
747 doi:10.1073/pnas.1703155114
- 748 Schoffelen, J.M., Oostenveld, R., Lam, N.H.L., Uddén, J., Hultén, A., Hagoort, P.,
749 2019a. A 204-subject multimodal neuroimaging dataset to study language
750 processing. *Sci. Data* 6, 17. doi:10.1038/s41597-019-0020-y
- 751 Schoffelen, J.M., Oostenveld, R., Lam, N.H.L., Udden, J., Hultén, A.H., Hagoort, P.,
752 2019b. Mother of unification studies, a 204-subject multimodal neuroimaging
753 dataset to study language processing. Donders Repository.
- 754 Valk, S.L., Xu, T., Margulies, D.S., Kahrabian Masouleh, S., Paquola, C., Goulas, A.,
755 Kochunov, P., Smallwood, J., Yeo, B.T.T., Bernhardt, B.C., Eickhoff, S.B., 2020.
756 Shaping brain structure: genetic and phylogenetic axes of macro scale
757 organization of cortical thickness. *BioRxiv*. doi:10.1101/2020.02.10.939561
- 758 Van Essen, D.C., Glasser, M.F., Dierker, D.L., Harwell, J., Coalson, T., 2012.
759 Parcellations and hemispheric asymmetries of human cerebral cortex analyzed
760 on surface-based atlases. *Cereb. Cortex* 22, 2241–2262.
761 doi:10.1093/cercor/bhr291
- 762 Van Veen, B.D., van Drongelen, W., Yuchtman, M., Suzuki, A., 1997. Localization of
763 brain electrical activity via linearly constrained minimum variance spatial filtering.
764 *IEEE Trans. Biomed. Eng.* 44, 867–880. doi:10.1109/10.623056
- 765 Voytek, B., Canolty, R.T., Shestyuk, A., Crone, N.E., Parvizi, J., Knight, R.T., 2010.
766 Shifts in gamma phase-amplitude coupling frequency from theta to alpha over
767 posterior cortex during visual tasks. *Front. Hum. Neurosci.* 4, 191.
768 doi:10.3389/fnhum.2010.00191

- 769 Wagstyl, K., Larocque, S., Cucurull, G., Lepage, C., Cohen, J.P., Bludau, S., Palomero-
770 Gallagher, N., Lewis, L.B., Funck, T., Spitzer, H., Dickscheid, T., Fletcher, P.C.,
771 Romero, A., Zilles, K., Amunts, K., Bengio, Y., Evans, A.C., 2020. BigBrain 3D
772 atlas of cortical layers: Cortical and laminar thickness gradients diverge in
773 sensory and motor cortices. *PLoS Biol.* 18, e3000678.
774 doi:10.1371/journal.pbio.3000678
- 775 Wagstyl, K., Ronan, L., Goodyer, I.M., Fletcher, P.C., 2015. Cortical thickness
776 gradients in structural hierarchies. *Neuroimage* 111, 241–250.
777 doi:10.1016/j.neuroimage.2015.02.036
- 778 Wang, X.-J., 2010. Neurophysiological and computational principles of cortical rhythms
779 in cognition. *Physiol. Rev.* 90, 1195–1268. doi:10.1152/physrev.00035.2008
- 780 Zhang, H., Watrous, A.J., Patel, A., Jacobs, J., 2018. Theta and alpha oscillations are
781 traveling waves in the human neocortex. *Neuron* 98, 1269–1281.e4.
782 doi:10.1016/j.neuron.2018.05.019
- 783
- 784

785 **Figure Legends:**

786 **Figure 1. Spatial gradient of peak frequency (PF) across the human cortex follows the posterior-**
787 **anterior hierarchy.**

788 (A) Estimating the power spectrum for each cortical region, and identifying peak frequencies after fitting
789 and subtracting the arrhythmic 1/f component. (B) Top-left panel shows the distribution of PF as a function
790 of the ROI's location along the y-axis of the coordinate system (posterior to anterior). Each point represents
791 the trimmed mean across participants of the PF for one ROI ($r = -0.84$, $p << 0.001$). Points are colored
792 according to their Z coordinates. Bottom panel: distribution of trimmed mean PFs across 384 cortical ROIs.
793 Top-right panel: Individual level correlation values computed between PF and y-coordinates across ROIs
794 (significant for 84% of participants, $p < 0.05$) and their consistency across all individuals (t -value = -15.52,
795 $p < 0.001$). (C) Top panel: t-values obtained from linear mixed effect modeling of PF as a function of the
796 coordinates of the ROI centroids. Bottom panel: cortical map of the corresponding fixed effect parameters
797 (see equation 2 for details). (D) Top-left panel: correlation between trimmed mean PF and geodesic
798 distance ($r = -0.89$, $p << 0.001$). Top-right panel: individual correlation values (significant for 88% of
799 participants, $p < 0.05$) and their consistency across all individuals (t -value = -17.32, $p < 0.001$). Bottom
800 panel illustrates geodesic distance values mapped on the cortical surface. Geodesic distance was
801 computed between centroid of all ROIs and the centroid of V1 and used this as a new axis to explain the
802 posterior-anterior direction in the cortex. (E) LMEM of PF as a function of geodesic distance performed,
803 separately, for all cortical ROIs, posterior-parietal ROIs ($Y < -43$ mm), central ROIs ($-43 < Y < 13$), and
804 frontal ROIs ($Y > 13$). To assess the distribution of PF along the posterior-anterior axis while accounting
805 for the inter-individual variability, LMEM was applied between the PF as a response variable and the
806 geodesic distance values as an independent variable, and identified a highly significant gradient of PF
807 along the specified geodesic distance ($t = -18.9$, $p << 0.001$). Furthermore, to test whether the spatial
808 gradient of PF constantly exists in different areas of the cortex, the cortical surface was split to 3 equal,
809 consecutive and non-overlapping windows (about 4 cm) based on its Y axis. For each window, LMEM was
810 applied between PF and geodesic distance, and found a significant gradient (window 1: $t = -8.1$, window
811 2: $t = -10.9$, window 3: $t = -5.2$, all $p < 0.001$). Indeed, our analysis demonstrates a significant organization
812 of PF along the posterior-anterior direction for all windows indicating that this axis constitutes a systematic
813 and constant gradient of PF.

814 Figure 1–figure supplement 1: Stability of the PF gradient over time

815 Figure 1–figure supplement 2. Within- and between-participant variability of ROIs' size and their impact on
816 PF gradient

817 **Figure 2. Spatial distribution of 1/f components (offset and slope) across human cortex.**

818 (A) Top panel: t-values obtained from linear mixed effect modeling of 1/f offset as a function of the
819 coordinates of ROI centroids. Bottom panel: cortical map of the corresponding fixed effects. (B) LMEM was
820 applied on 1/f slope, analogous to the 1/f offset. The slope and offset of 1/f component were estimated for
821 each ROI and participant, using the FOOOF package (see methods section for further details). (C)
822 Correlation between trimmed mean PFres (187 participants, 384 ROIs) and ROI's location along the y-axis
823 (posterior to anterior) ($r = -0.63$, $p << 0.001$). The residual PF scores (PFres) were obtained after regressing
824 out the contribution of 1/f offset and slope values (fixed effect) from PF, using LMEM. (D) t-values obtained
825 from linear mixed effect modeling of PF as a function of the coordinates of the ROI centroids (LMEM; t-
826 values: $Y = -8.3$, $Z = -4.3$, $Y:Z = -16$; all $p < 0.001$). The cortical maps show the corresponding fixed effects.

827 **Figure 3. Spatial gradient of cortical thickness along the posterior-to-anterior direction.**

828 Top panel: correlation between mean cortical thickness and ROI's location along the y-axis (posterior to
829 anterior) ($r = -0.84$, $p << 0.001$). Bottom panel: cortical map of trimmed mean PF across 384 cortical ROIs.

830 *Figure 3–figure supplement 1.* Relationship between PF (187 participants, 384 ROIs) and CT, after
831 regressing out the effect of ROI coordinates.

832 *Figure 3–figure supplement 2.* Relationship between PF (187 participants, 384 ROIs) and CT.

833 **Figure 4. PF and CT variation along the cortex follows anatomical hierarchies.**

834 (A) Top panel: Schematic representation of seven regions (V1, V2, V4, MT, DP, TEO, 7A) used for defining
835 visual hierarchy. Bottom panel: Each bar shows the fixed effect of the LMEM where the PF/CT was defined
836 as a response variable and the visual hierarchy as an independent variable. We found a significant
837 decrease of PF ($t = -10.1$, $p << 0.001$) but a significant increase of CT ($t = 54.9$, $p << 0.001$) along the
838 visual hierarchy. To impose the hierarchical order of the seven ROIs in an LMEM, we defined a seven-
839 element hierarchy vector for each participant and hemisphere ($V = [1, 2, 3, \dots, 7]$), whose elements refer
840 to the hierarchical level of the corresponding ROI. The random effect was specified as in equation 1. PF/CT
841 values were standardized before LMEM analysis. This model tests the significance of PF/CT changes
842 along the specified hierarchy. (B) Fixed effect per network obtained from linear mixed effect modeling of
843 CT (top panel) and PF (bottom panel) as a function of networks (independent variable), where networks

were specified as a categorical variable. The random structure was defined as in equation 1. Fixed effect per network indicates the effect of that network on PF/CT. The network variable was defined as a categorical variable by assigning cortical regions to eight functional resting-state networks comprising three sensory ('VIS', visual; 'AUD', auditory; and 'SOM', somatomotor) and five association ('DAN', dorsal 670 attention; 'FPN', frontoparietal; 'VAN', ventral attention; 'DMN', default mode; and 'CON', cingulo-849 opercular) networks. We applied ANOVA on LMEM fit and computed F-stat for the fixed effect. (PF: F-stats 850 = 264, $p << 0.001$; CT: F-stats = 746, $p << 0.001$). PF values were significantly lower in association RSNs 851 (except for DAN) than in sensory RSNs ($t = -11.1$, $p << 0.001$), whereas CT values were significantly higher 852 in association RSNs than in sensory RSNs ($t = 14.1$, $p << 0.001$). Error bar indicates the lower and upper 853 bounds of LMEM for the fixed effect.

Figure 4—figure supplement 1. Distribution of location independent PF (PFres) among resting state 854 networks.

Figure 4—figure supplement 2. Distribution of location independent CT (CTres) among resting state 855 networks.

858 **Figure 5. Histogram of spectral peaks.**

Histogram of all detected spectral peaks (across ROIs and participants) delineates the classical frequency 859 bands used in the EEG and MEG literature (theta 3.5–7.5 Hz, alpha 8.5–13 Hz, low-beta 15–25 Hz and 860 high-beta 27.5–34).

862 **Figure 6. Spatial gradients of band-specific PFs across human cortex follows the posterior-anterior 863 direction.**

(A, B, and C) Top panel: Dependency between the trimmed mean of band-specific PF (187 participants, 864 384 ROIs) and the ROI's location along the y-axis (posterior to anterior) for theta ($r = 0.4$, $p < 0.001$), alpha 865 ($r = -0.87$, $p < 0.001$), and beta ($r = 0.9$, $p < 0.001$) bands, respectively. Points are colored according to 866 their Z coordinates. Bottom panel: distribution of trimmed mean band-specific PFs across 384 cortical 867 ROIs. (D, E, and F) Top panel: t-values obtained from linear mixed effect modeling of band-specific PF 868 (theta, alpha, and beta bands, respectively) as a function of the coordinates of the ROI centroids. Bottom 869 panel: cortical map of the corresponding fixed effect parameters (see equation 2 for details).

Figure 6—figure supplement 1. Spatial gradients of band-specific PF across the cortex after factoring out 871 the impact of 1/f components (offset and slope)

873 Figure 6—figure supplement 3. Dependency between band-specific PF and CT

874 **Figure Supplement Legends:**

875 **Figure 1—figure supplement 1: Stability of the PF gradient over time**

876 PF gradient along the posterior-anterior direction computed for 1st and 2nd halves after splitting the time
877 course to two equal segments. (A) Top panels: correlation between trimmed mean PF (187 participants,
878 384 ROIs) and ROI's location along the y-axis (posterior to anterior) computed for the first ($r = -0.82$, $p <$
879 0.001) and second ($r = -0.81$, $p < 0.001$) halves of the time course. Points are colored according to their Z
880 coordinates. Bottom panel: trimmed mean PF values mapped on the cortex surface. (B) T-values obtained
881 from linear mixed effect modeling of PF as a function of coordinates of the ROI centroids, obtained from
882 the first half (top panel) and the second half (bottom panel) of the time course. Cortical maps below each
883 table shows the fixed effects of the LMEM. (C) Linear mixed effect modelling of PF as a function of the
884 time and centroid coordinates. We defined the time as a categorical variable ('1st half', '2nd half') and
885 added it to our LMEM, where we defined PF as a function of centroid coordinates, their interactions and
886 time. The statistical model showed a non-significant effect of time ($t = -1$, $p > 0.05$) on our results. This
887 analysis shows that the spatial gradient of PF along the posterior-anterior direction is stable over time.

888 **Figure 1—figure supplement 2: Within- and between-participant variability of ROIs' size and their
889 impact on PF gradient**

890 (A) histogram of ROIs' size for a given participant. (B) Bar plots depicting the between-participant
891 variability of the ROIs' area. Bars represent the mean and error bars show the standard deviation of a
892 given ROI's cortical area across all participants. In our main analysis, we down-sampled the individual
893 cortical surfaces to 8196 vertices and 16384 (triangular) faces and co-registered to a finer version of
894 Conte69 atlas. The atlas provides anatomical labels for each vertex but not for the faces. To obtain the
895 area of a given ROI, we first assigned a label to each face based on the label of the nearest vertex
896 (Euclidean distance was computed between centroid of the given face and all vertices) and summed across
897 the area values of the identically labeled faces. (C) To assess the impact of ROI size on spatial gradient
898 of PF, we used an LMEM according to equation (1) of the manuscript where we included ROIs' size as an
899 additional fixed effect variable. We found no significant impact of ROIs' size on spatial gradients of PF
900 along the Z and Y axes (ROI size: $t = 1.5$, $p > 0.05$; Y: $t = -15.2$, Z: $t = -9.9$, Y:Z: $t = -31$).

901 **Figure 3—figure supplement 1: Relationship between PF (187 participants, 384 ROIs) and CT, after
902 regressing out the effect of ROI coordinates.**

903 We factored out the impact of ROI coordinates (x,y,z) from both PF and CT using LMEM according to
904 equation (1), and obtained the residuals, PFres and CTres. These residuals describe individual spatial
905 variations of PF and CT that cannot be explained by a linear model of their spatial location. We again
906 applied LMEM defining PFres as a function of CTres and found a significant relationship (LMEM: $t = -6.9$,
907 $p << 0.001$). The scatter plot represents the relationship between the mean PFres and the mean CTres
908 across cortical ROIs. This significant relationship demonstrates that they are more directly related to each
909 other than can be explained by their individual dependency on location (x,y,z). This result proposes that
910 peak frequency is related to structural features that likely represent cortical hierarchies.

911 **Figure 3–figure supplement 2: Relationship between PF (187 participants, 384 ROIs) and CT.**

912 The scatter plot represents the dependency between the trimmed mean PF and the trimmed mean-CT and
913 their correlation ($r = -0.14$, $p < 0.001$). This low correlation (although very significant) actually reflects the
914 fact that correlation analysis is not optimal in this case. It does not take into consideration the variability
915 between participants (e.g. the fact that some participants have an overall higher occipital alpha frequency
916 compared to others). This is also one of the reasons for the large scattering of values in the plot. Therefore,
917 LMEM is the preferred statistical tool because it models specifically the inter-individual differences and, as
918 a result, leads to more robust and highly significant results.

919 **Figure 4–figure supplement 1. Distribution of the location independent PF (PFres) among resting
920 state networks.**

921 T-values obtained from linear mixed effect modeling of the location independent PF among resting state
922 networks. The network variable was defined as described in Figure 4. Here, we asked the question of
923 whether the PF differs between resting state networks irrespective of its location? To answer this, we first
924 regressed out from PF the changes that can be explained by linear dependencies on x,y,z, using LMEM,
925 and again performed LMEM analysis (between PF and networks) as described for Figure 4. Interestingly,
926 we found a significant difference among networks for PF. This was the case when looking at the standard
927 resting-state networks and also when testing sensory against association areas. These results indicate
928 that, beyond a global effect of location, networks still differ significantly in PF after removing the linear
929 effects of location.

930 **Figure 4–figure supplement 2. Distribution of location independent CT (CTres) among resting
931 state networks.**

932 Similar to Figure 4 - figure supplement 1, LMEM was performend on CT values, and found a significant
933 difference between network. This result turns out that the significant impact of networks on CT is
934 independent of location.

935 **Figure 6–figure supplement 1: Spatial gradients of band-specific PF across the cortex after
936 factoring out the impact of 1/f components (offset and slope)**

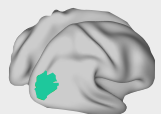
937 (A) Top panel: Scatter plots representing the relationship between trimmed mean PFres (187 participants,
938 384 ROIs) and ROI's location along the y-axis for theta band ($r = 0.3$, $p < 0.001$), together with
939 corresponding cortical map of trimmed mean PFres. Panels (B) and (C) show the same results for alpha
940 ($r = -0.77$, $p < 0.001$), and beta ($r = 0.78$, $p < 0.001$) frequency ranges. The residual PF scores (PFres)
941 were obtained after regressing out the contribution of 1/f offset and slope values (fixed effect) from band-
942 specific PF, using LMEM. (D) Top panel: t-values obtained from linear mixed effect modeling of band-
943 specific PFres as a function of the coordinates of the ROI centroids for theta band (LMEM; t-values: $Y = 7$,
944 $Z = -8.6$, $Y:Z = -8.3$; all $p < 0.001$). Bottom panel: cortical map of the corresponding fixed effect parameters
945 (see equation 2 for details). Similarly, panels (E) and (F) show the results for alpha (LMEM; t-values: $Y =$
946 -7.8 , $X:Z = -4$, $Y:Z = 8.9$; all $p < 0.001$), and beta (LMEM; t-values: $Y = 6.7$, $Y:Z = 6.8$; all $p < 0.001$)
947 frequency ranges, respectively. These analyses demonstrate that the spatial gradient of band-specific PFs
948 is independent of spatial changes of 1/f slope and offset.

949 **Figure 6–figure supplement 2: Dependency between band-specific PF and CT**

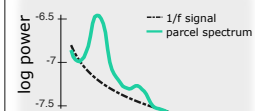
950 Scatter plots show the relationship between trimmed mean band-specific PF and mean CT for theta (A),
951 alpha (B), and beta (C) frequency ranges. Robust correlation was computed between trimmed mean band-
952 specific PF and mean CT. LMEM was applied across all cortical regions defining individual band-specific
953 PF as a function of individual CT (fixed effects) while accounting for between-individual variability (random
954 effect. Both correlation and LMEM analyses identified a significant positive relationship for theta and beta
955 bands but a significant negative relationship for alpha band. This analysis shows that the dependency
956 between PF and CT is frequency specific.

Figure 1

A Example:
Identifying PFs for
Brodmann area 19



subtracting 1/f
from spectrum



Identifying peaks
from residual



Identifying the PF

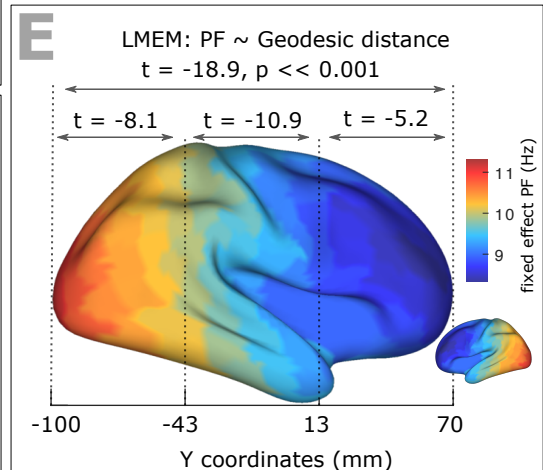
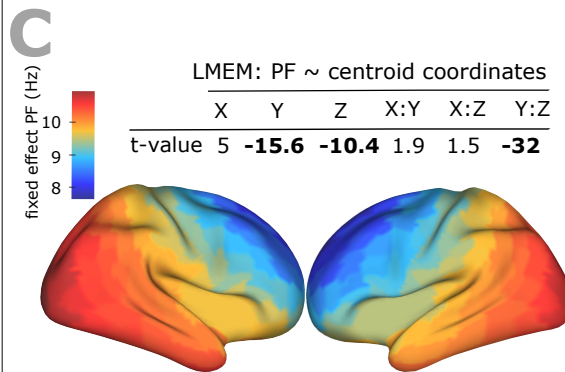
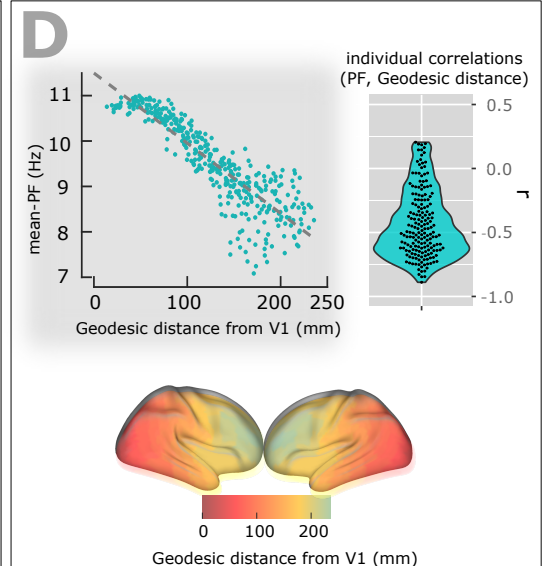
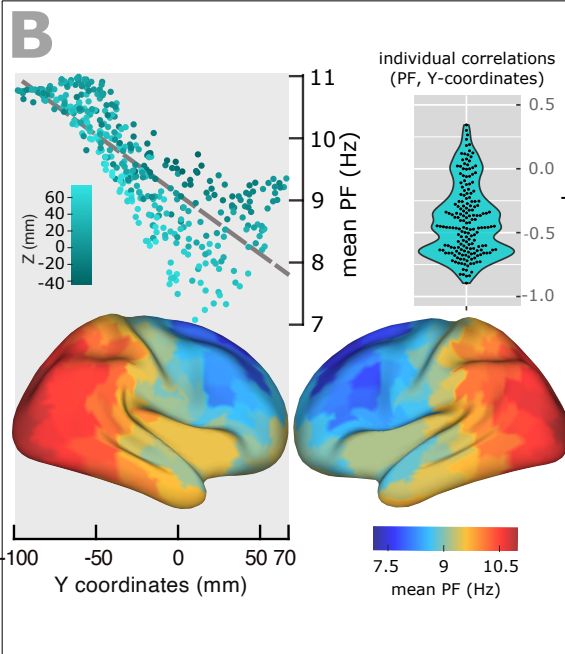
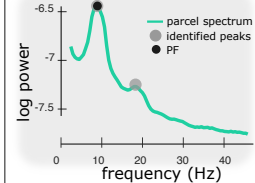
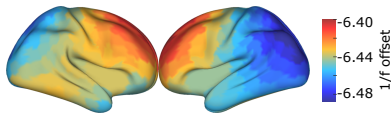


Figure 2

A

LMEM of $1/f$ offset

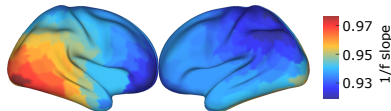
	X	Y	Z	X:Y	X:Z	Y:Z
t	1.4	2.8	3.5	-5.8	0.5	13.2



B

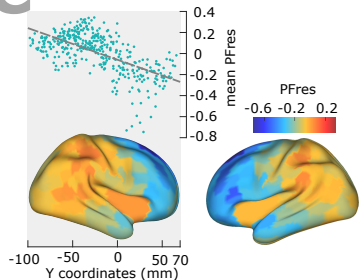
LMEM of $1/f$ slope

	X	Y	Z	X:Y	X:Z	Y:Z
t	1.3	-4.3	-1.2	-6.8	0.9	6.9



C

Mean PFres



D

LMEM of PF after regressing out the $1/f$

	X	Y	Z	X:Y	X:Z	Y:Z
t	4.3	-8.3	-4.3	5.7	0.5	-16

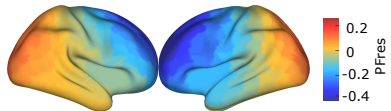


Figure 3

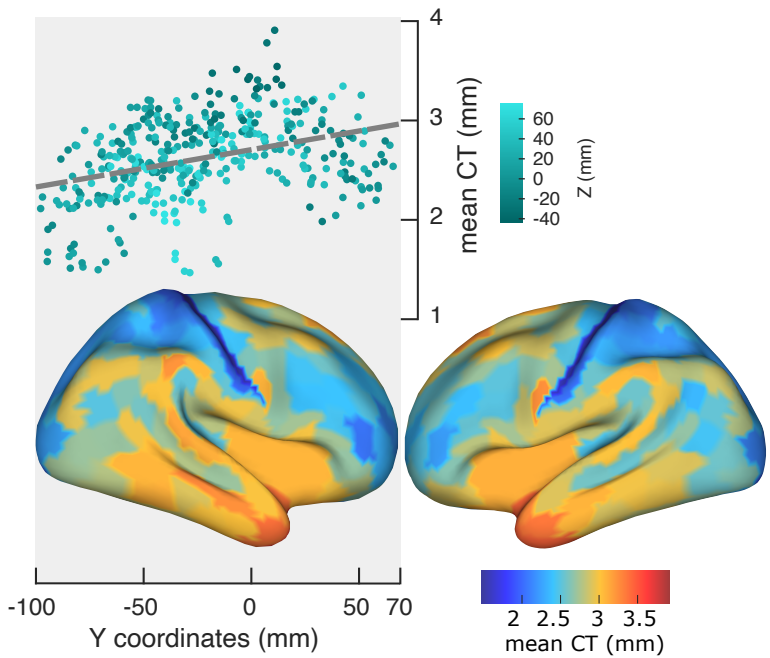


Figure 4

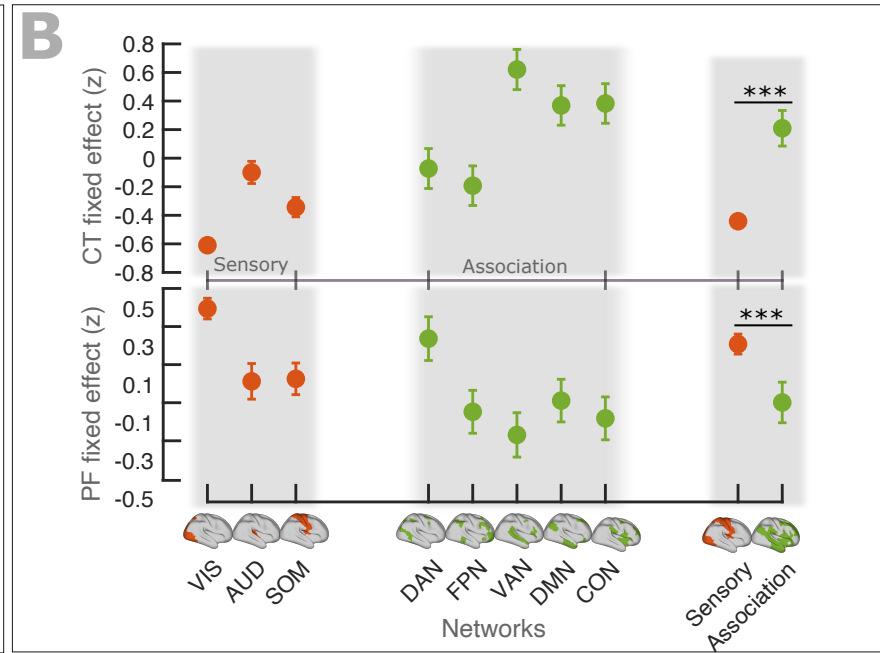
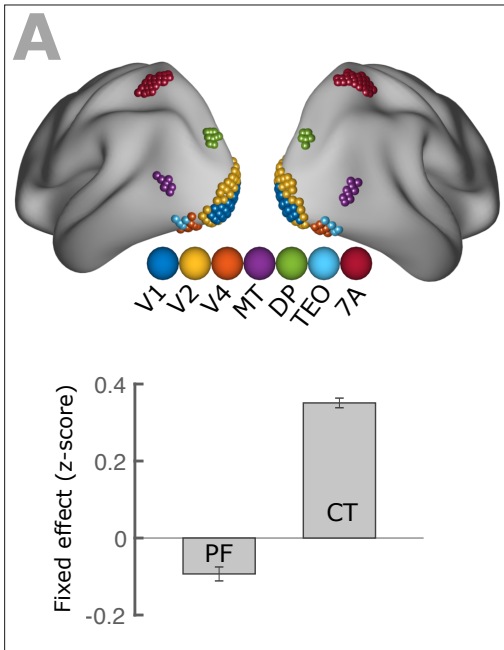


Figure 5

spectrum peaks, entire cortex

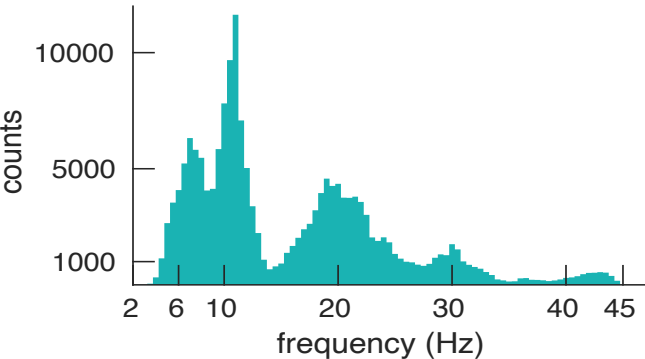
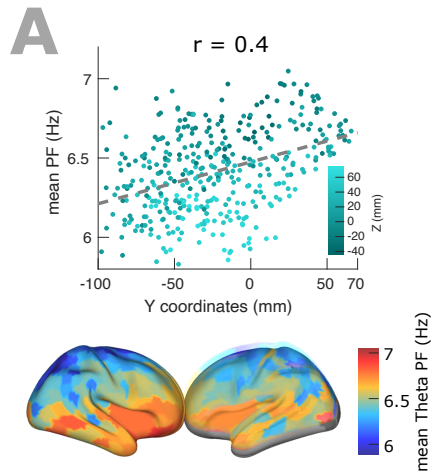
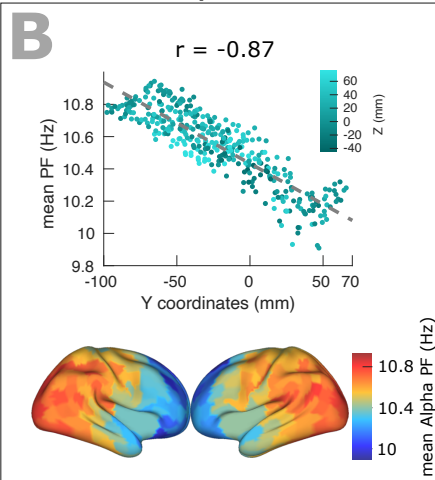


Figure 6

Theta



Alpha



Beta

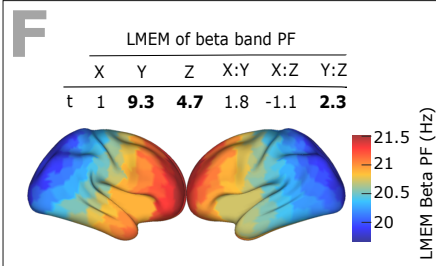
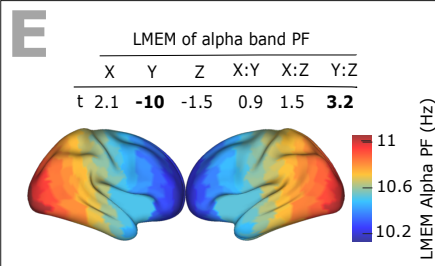
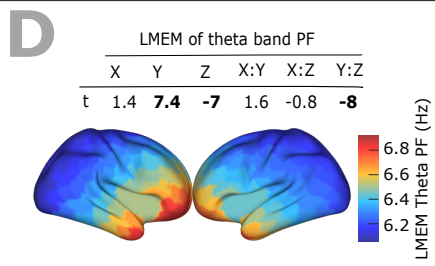
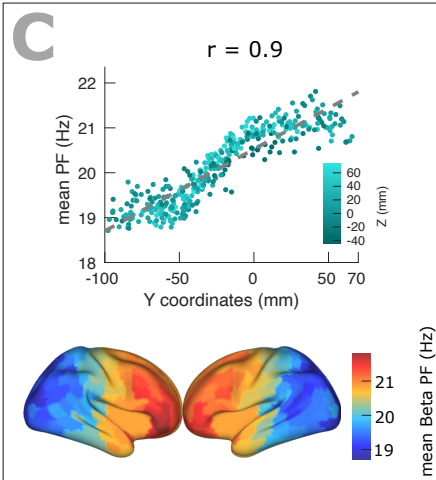


Figure 1-figure supplement 1

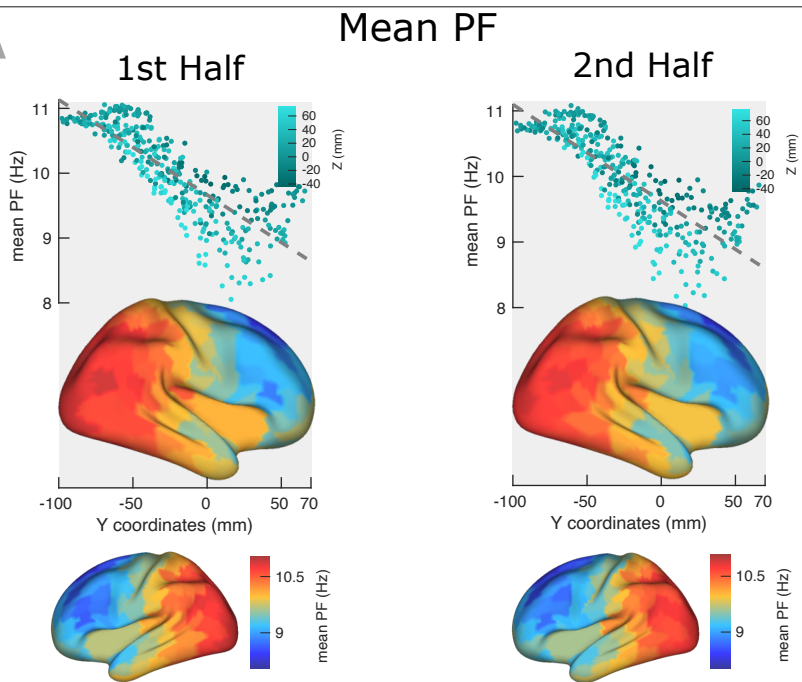
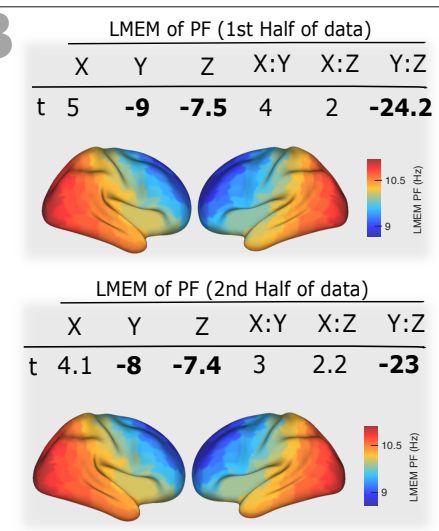
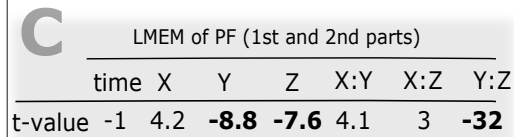
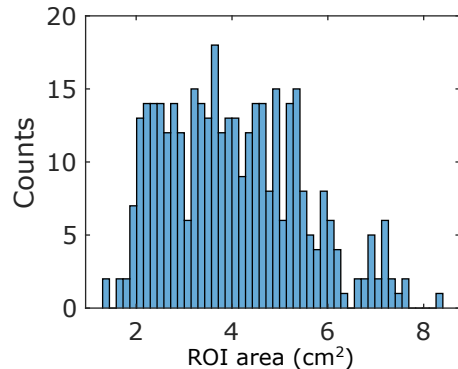
A**B****C**

Figure 1-figure supplement 2

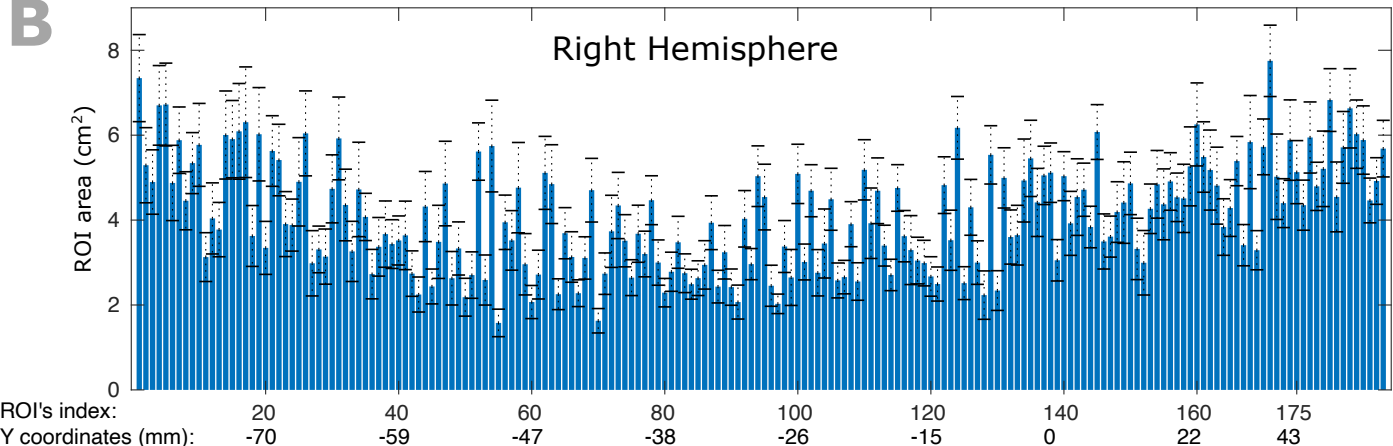
A



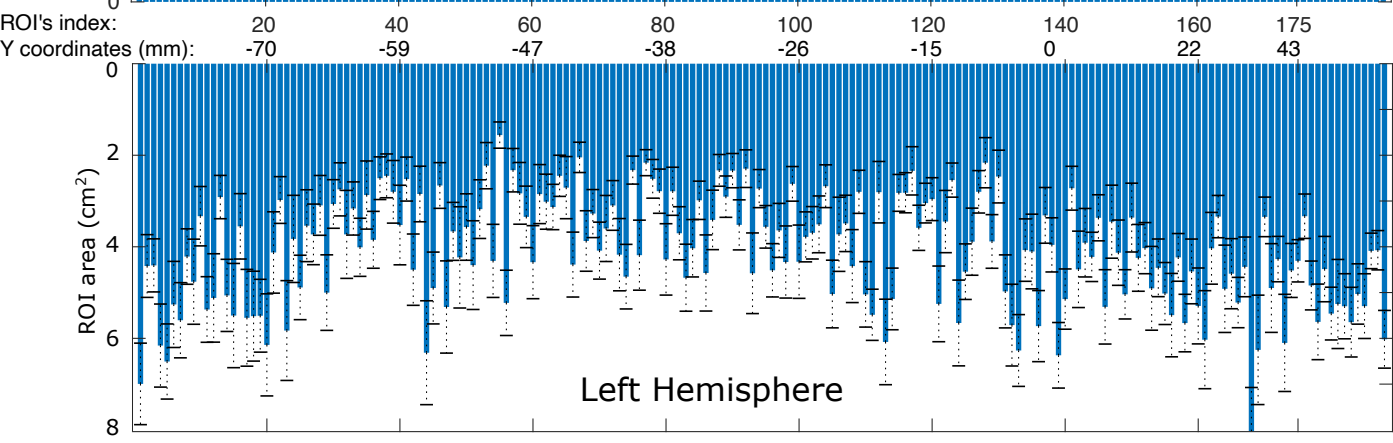
C

LMEM: PF ~ ROI area + ROI coordinates							
ROI area	X	Y	Z	X:Y	X:Z	Y:Z	
t-value	1.5	5	-15.2	-9.9	2.9	1.5	-31.2

B



Right Hemisphere



Left Hemisphere

Figure 3-figure supplement 1

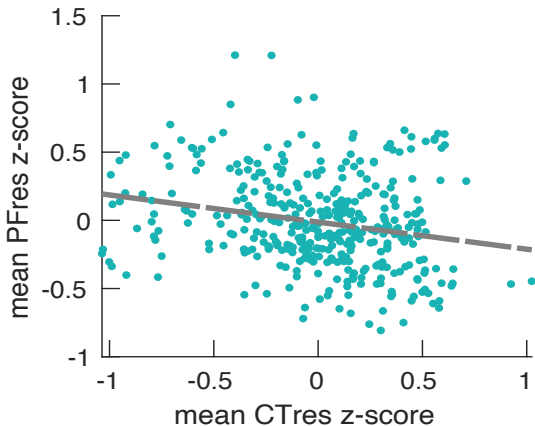


Figure 3-figure supplement 2

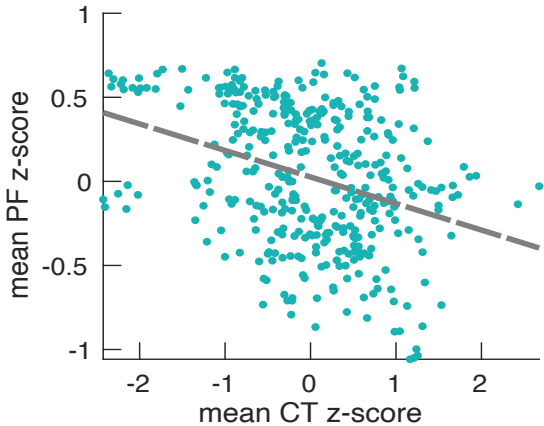


Figure 4-figure supplement 1

LMEM: PFres ~ Resting State Networks

	SOM	CON	DAN	VAN	FPN	AUD	DMN
t-value	1.6	0.8	2.5	-2.4	1.8	0.6	3.2

ANOVA, F-value = **26**, $p << 0.001$

Figure 4-figure supplement 2

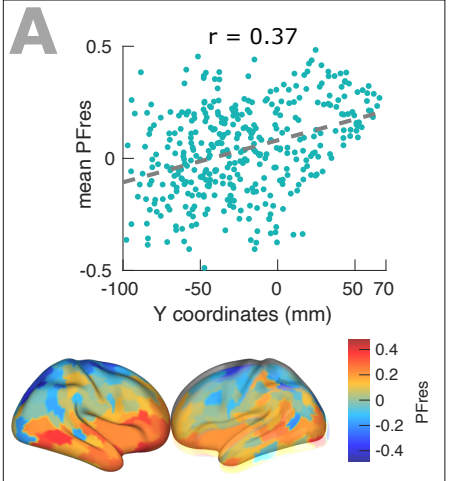
LMEM: CTres ~ Resting State Networks

	SOM	CON	DAN	VAN	FPN	AUD	DMN
t-value	23	60	34	57	10	11	48

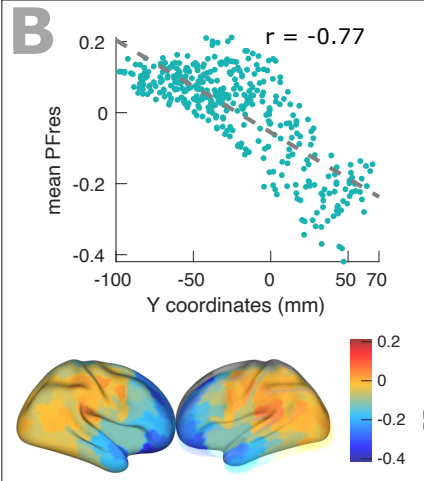
ANOVA, F-value = **949**, p << 0.001

Figure 6-figure supplement 1

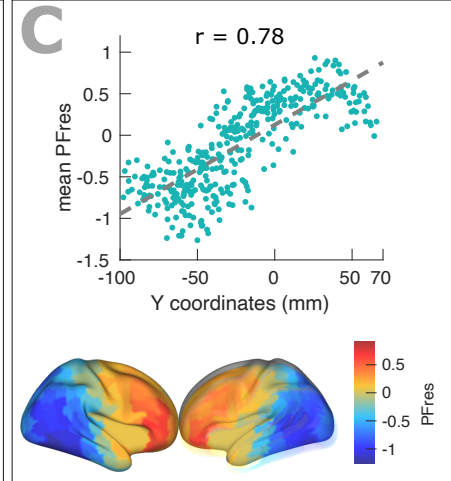
Theta



Alpha



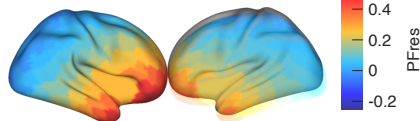
Beta



D

LMEM of theta PFres

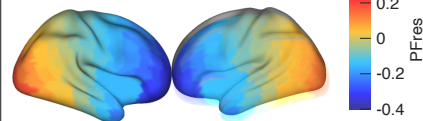
	X	Y	Z	X:Y	X:Z	Y:Z
t	2.6	7	-8.6	5.2	-0.8	-8.3



E

LMEM of alpha PFres

	X	Y	Z	X:Y	X:Z	Y:Z
t	-0.2	-7.8	-1.5	-1.4	-4	8.9



F

LMEM of beta PFres

	X	Y	Z	X:Y	X:Z	Y:Z
t	0.6	6.7	2.3	2.1	-1.5	6.8

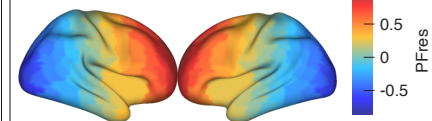
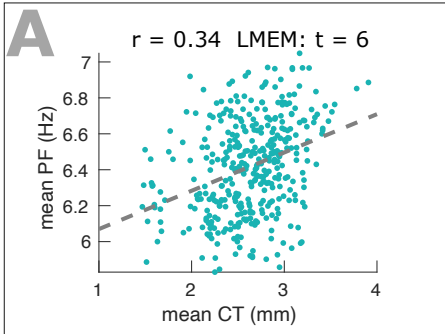
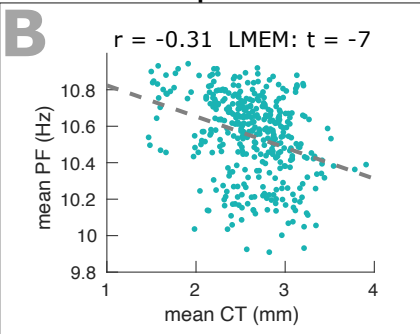


Figure 6-figure supplement 2

Theta



Alpha



Beta

